JACS
JOURNAL OF THE AMERICAN CHEMICAL SOCIETY
pubs.acs.org/JACS
Article

A Cation-Tethered Flowable Polymeric Interface for Enabling Stable Deposition of Metallic Lithium

Zhuojun Huang,[⊥] Snehashis Choudhury,*[,⊥] Huaxin Gong, Yi Cui,* and Zhenan Bao*

Cite This: J. Am. Chem. Soc. 2020, 142, 21393−21403

ABSTRACT: A fundamental challenge, shared across many energy storage devices, is the complexity of electrochemistry at the electrode−electrolyte interfaces that impacts the Coulombic efficiency, operational rate capability, and lifetime. Specifically, in energy-dense lithium metal batteries, the charging/discharging process results in structural heterogeneities of the metal anode, leading to battery failure by short-circuit and capacity fade. In this work, we take advantage of organic cations with lower reduction potential than lithium to build an electrically responsive polymer interface that not only adapts to morphological perturbations during electrodeposition and stripping but also modulates the lithium ion migration pathways to eliminate surface roughening. We find that this concept can enable prolonging the long-term cycling of a high-voltage lithium metal battery by at least twofold compared to bare lithium metal.

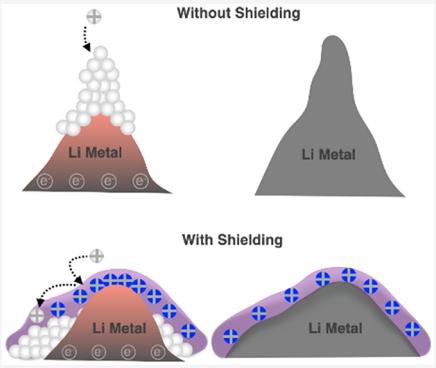

INTRODUCTION

Advancements in emerging automobiles and electronic devices rely on the fundamental and technological development in energy storage capabilities. The development of lithium ion batteries (LIB) has proven to be a paradigm shift in several applications ranging from portable electronics to electric transportation to renewable energy storage.[1−6] However, the increased demands from these applications call for specific energy and energy density higher than graphitic anodes based LIBs. It is well-known that the replacement of graphite anode with a metallic lithium can significantly boost the anode-specific capacity from 372 to 3860 mAh g^{-1}, in addition to the possibilities of utilizing lithium-free cathodes like sulfur or oxygen.[7−13]

The lithium metal batteries (LMB), which are considered as the "Holy Grail" of future Li-based batteries, are yet to be widely adopted for commercialization due to battery short-circuits and poor cycle life. These issues are rooted in the unstable interface between lithium metal anode and the electrolyte. The highly reactive lithium metal forms a layer of insulating solid−electrolyte interface (SEI) when exposed to liquid electrolyte. The intrinsic mechanical brittleness of this SEI layer and the large volumetric change during lithium cycling result in the fracture of the SEI layer and the formation of an uneven SEI.[8,10,14−17] The roughened anodic surface causes electric field localization at the surface irregularities. This results in a heterogeneous nucleation and deposition of lithium metal during the electrodeposition (charging) process. This process is naturally self-amplifying, as irregular lithium deposition serves as the new heterogeneous nucleation site.[8−10] Without intervention, the battery will face a cascade of failure mechanisms like dendritic growth and enhanced electrolyte decomposition.

Many past works have attempted to address the aforementioned interfacial instabilities using a variety of approaches such as nano/microstructures that geometrically confine the lithium metal to reduce the volumetric changes during charge and discharge,[18−25] electrolyte mixture modifications,[26−29] chemical additives in the electrolytes to promote the formation of a mechanically robust SEI layer,[30−38] tuning solvation structures of liquid electrolyte solvents,[26,29,39,40] sacrificial coatings and other lithium metal pretreatment to alter the nucleation and deposition dynamics,[41−45] and so forth. A commonality in these approaches is the deliberate modification of the interfacial chemistry, morphology, or mechanics using an artificial SEI layer to enable fast and uniform ion transport and facilitate reversible volume changes during lithium metal plating and stripping.[46−51] Although many of these methods have proven effective, the problem of Li metal anode interfacial stability is still not yet solved, and the understanding of the underlying physical−chemical complexities is still limited.

We hypothesize that an effective method to address the lithium anodic interfacial instability is to fundamentally alter the lithium ion deposition pathways by electrostatically blocking the heterogeneous surface regions that concentrate lithium ions due

Received: September 8, 2020
Published: December 14, 2020

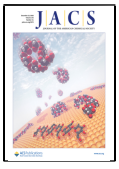

https://dx.doi.org/10.1021/jacs.0c09649
J. Am. Chem. Soc. 2020, 142, 21393−21403

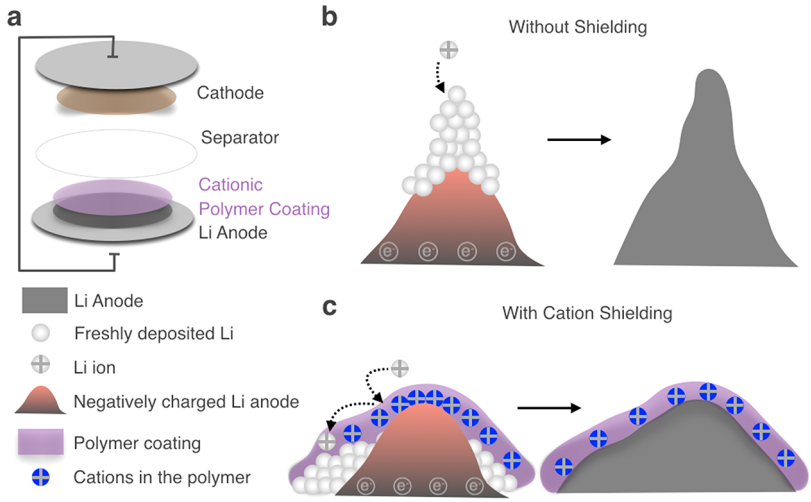

Figure 1. Polyionic liquid (PIL) as the anodic coating for lithium metal batteries: (a) lithium metal battery with polymer-coated anode; (b) the concentrated electric field at the vicinity of surface protrusions causing the self-amplifying dendritic deposition of lithium ions; (c) PIL coating on lithium metal anode. During Li^+ deposition, cations in the PIL coating remain electrochemically stable and can effectively shield the Li^+ ions, resulting in flatter and more homogeneous deposition.

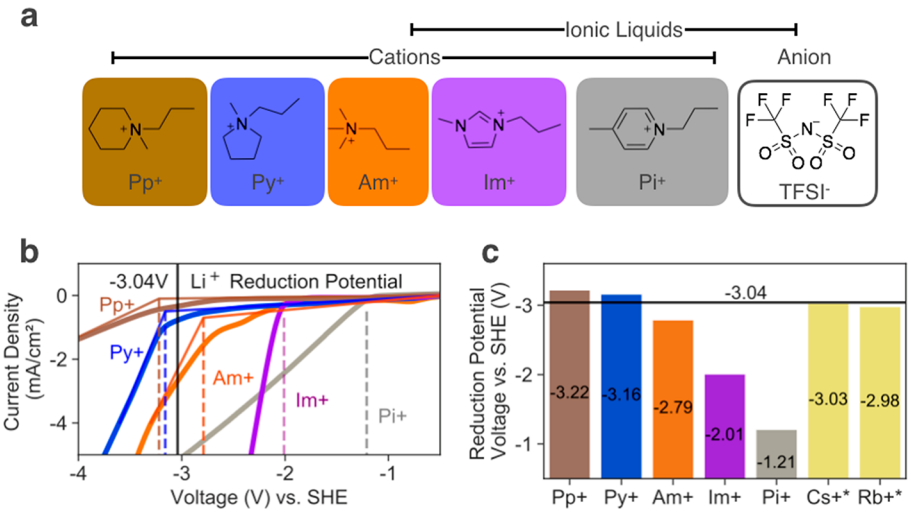

Figure 2. Reduction potential of organic cations. (a) Chemical structures of organic salts in this study. They are composed of $TFSI^-$ anion and various cations (Pp^+, brown; Py^+, blue; Am^+, orange; Im^+, purple; Pi^+, gray). (b) *I*−*V* curve: current density recorded when voltage was linearly swept from 0 to −6 V using the organic salts. The voltage is referenced to standard hydrogen electrode (SHE). The dashed line marks the voltage where the slope of the *I*−*V* curve deviated corresponding to the reduction potential of the cations. (c) Bar chart comparing the reduction potential of organic cations (measured) and metallic cations (*[52,55]) to that of Li^+ (marked by the line).

to a high electric field. This can be experimentally implemented using electro-inactive cations at the interface that can "shield" the inhomogeneous protrusion on the electrode surface to neutralize the electric field landscape. However, this strategy can be successful only when it is ensured that these electro-inactive cations do not undergo reduction during the lithium deposition process. In other words, their reduction potential needs to be even lower than that of Li^+ ions that already have the lowest intrinsic reduction potentials among metallic cations. Previously Ding and co-workers[52] pointed out that Cs^+ can achieve lower reduction potential than Li^+ by tuning its concentration based on the Nernst equation. Furthermore, it was shown that the addition of Cs^+ ions in an electrolyte resulted in improved lithium deposition morphology and battery operation.[52] However, the concentration-dependent electrochemical stability of Cs^+ ions can be undermined by their localized aggregation at the electrode surface, resulting in the reduction of Cs^+.

Instead of using free cations, here we propose to tether the cations onto a polymer backbone to form a polyionic liquid (PIL) coating which would homogenize the electric field distribution on the electrode surface and promote uniform lithium deposition. Incorporation of such cations in a polymer coating on the lithium anode is a facile method that does not alter existing manufacturing capabilities and also limits their interaction with other battery components. Building on previous studies on anodic coating using polymers like poly(ethylene oxide) (PEO),[53] poly(dimethylsiloxane) (PDMS),[54] Nafion,[48] single-ion conducting polymer,[46] and poly(vinylidene fluoride) (PVDF),[31] the interfacial material in this work is designed to be chemically inert with lithium, possess a conducting pathway for lithium conduction, and be mechanically robust for adapting to rapid volume changes. We show that the PIL interface is chemically stable even at ultranegative potentials of lithium reduction (<−3.04 V vs SHE) and results in improved lithium

https://dx.doi.org/10.1021/jacs.0c09649
J. Am. Chem. Soc. 2020, 142, 21393−21403

deposition morphology as well as superior cycling performance of a lithium metal battery.

RESULTS

Electrostatic Shielding with PIL Coating. The schematic of Figure 1a illustrates a lithium anode coated with a PIL containing electro-inactive cations. In the absence of any coating, the concentrated electric field at the surface protrusion triggers a self-amplified surface-roughening process of lithium deposition (Figure 1b). The presence of cations is hypothesized to neutralize the radiating electric field and helps to homogenize lithium deposition pathways. Figure 1c showcases the "cationic shielding" phenomenon where the presence of the PIL coating results in redistribution of Li^+ ions away from the surface protrusions leading to a more uniform topology. The physiochemical prerequisites of the PIL polymer coating for the cationic shielding mechanism are the following: (1) the cations in the PIL backbone should have a lower reduction potential than that of Li^+; (2) sufficient mobility of the polymer chains is essential for electric-field-based response of the cations. The following sections will discuss the experimental results and analysis to determine how a PIL meets these requirements.

Cations for Electrostatic Shielding. Here, we screen a plethora of cation structures to examine their reduction potential. Figure 2a shows the composition of organic salts examined in this study: the same anion bis(trifluoromethane) sulfonimide ($TFSI^-$) is paired with five different cations, piperidinium (Pp^+), pyrrolidinium (Py^+), ammonium (Am^+), imidazolium (Im^+), and pyridinium (Pi^+). These ionic liquids are synthesized in the lab, and their chemical structures are verified with hydrogen nuclear magnetic resonance spectroscopy (H NMR). The synthesis schematics and H NMR spectrum are shown in Supporting Information Figures 1−2. The reduction potentials of these salts are measured using linear sweep voltammetry from 0 to −6 V using a three-electrode setup composed of glassy carbon working, Pt counter, and Ag/AgCl reference electrodes in saturated KCl solution. As shown in Figure 2b, the corresponding reduction voltage (vs SHE) of these salts is assigned to the onset point of an abrupt increase in the anodic current. Figure 2c summarizes and compares the reduction potentials of organic cations measured in this study and two metallic cations Cs^+ and Rb^+, which have reduction potentials closest to lithium based on previous literature.[52,55] Interestingly, we find that the Pp^+ and Py^+ cations are stable up to potentials as low as −3.22 and −3.16 vs SHE, which are 0.18 and 0.12 V below lithium ion, respectively. To evaluate the effect of scanning voltage rate on the reduction potential of the system, reduction of Py^+TFSI^- ionic liquid was conducted at two different scan rates, as shown in Supporting Information Figure 3, and similar reduction onset voltage was observed. On the basis of these observations, we postulate that artificial interfaces comprised of these organic cations can be electrochemically stable even during lithium ion reduction ($Li^+ + e^- \rightarrow Li$).

Beyond electrochemical stability, maintaining chemical stability at the interface is also important for sustaining long-term battery operation. The growth in interfacial impedance of Li||Li symmetric cells comprised of ionic liquids as electrolytes is recorded as a function of time, which is known to be directly related to the extent of chemical reaction at the interface. Supporting Information Figure 4 shows that the interfacial resistance of Pp^+TFSI^- is highest among the different salts under study. On the contrary, other salts maintain a relatively stable interface over time after the initial formation of a passivating layer. The interfacial resistance after 70 h was in the following order: Pp^+TFSI^- > Am^+TFSI^- > Pi^+TFSI^- > Py^+TFSI^- > Im^+TFSI^-. Thus, on the basis of electrochemical and chemical stability analyses, we determine that Py^+TFSI^- salt is the ideal candidate for interface design.

To analyze the impedance buildup when lithium metal is in contact with the small molecules of ionic liquids, we assembled Li|Li symmetric cell with 70 μL of ionic liquid sandwich in the middle. The cell is rested at room temperature for 3 days before being disassembled, and the lithium surface is examined with X-ray photoelectron spectroscopy (XPS) to measure the chemical composition of the surface. The XPS analysis in Supporting Information Figure 5 revealed similar surface chemistry when lithium is in contact with Pp^+TFSI^-, Py^+TFSI^-, and Am^+TFSI^-. Based on the C 1s XPS results, the surface shows reaction products from both cation and anion breakdown (−C−SOx, C 1s, ∼289 eV, −C−S, C 1s, ∼286 eV). From the N 1s and S 2p profile of the lithium surface, we notice that Am^+TFSI^- has less products from $TFSI^-$ anion breakdown (−N−SOx, N 1s, ∼398 eV, −SOx, S 2p, 167 eV) and more product from lithium reduction (−Li−N, N 1s, 396.3 eV −LixS, S 2p, ∼162 eV). This is in accordance with our cyclic voltammetry measurement where Am^+TFSI^- has reduction potential lower than that of lithium ion, while Pp^+TFSI^- and Py^+TFSI^- have higher reduction potential.

Designing the PIL Interface. The PIL chemistry is proposed to be designed for effective inhibition of electrochemical instability on the lithium surface by incorporating Py^+TFSI^- small molecules while ensuring high mobility of the cationic polymer chains. As shown in Figure 3a, we use a free radical polymerization technique to synthesize polymers comprised of Py^+TFSI^- salts and fluorinated acrylic (FA) side chains in different ratios. The detailed synthesis methods are provided in Supporting Information Figures 6−7 and Supporting Information Table 1. The different ingredients of this polymer synergistically contribute to our design principle. The Py^+ cations modulate the lithium ion deposition pathway, and the counteranions ($TFSI^-$) form dynamic ionic bonds to enable polymer self-healing and viscoelasticity. The FA side chains are chemically stable and inert, and they can limit the electrolyte access to the lithium metal for undergoing side reactions. Additionally, the FA side chains also impart flowability to the polymer by lowering its glass transition temperature (Tg) and increasing segmental mobility. The relative content of ionic and fluorinated components in the polymer can influence the degree of mechanical and ionic properties. We systematically vary the ionic and fluorinated side chains in the backbone that resulted in large variations of the polymer mechanics from liquid to solid as shown in Supporting Information Figure 8. The PILs are named from 0 to 100, based on the molar percentage of Py^+TFSI^- side chains added to the polymerization reaction mixture.

The composition of PIL polymers was examined with hydrogen and fluorine nuclear magnetic resonance spectroscopy (^{1}H NMR and ^{19}F NMR), as shown in Figure 3b. The ^{19}F NMR displays all peaks in the spectra, and the full ^{1}H NMR spectra for various PILs are shown in Supporting Information Figure 9. In ^{1}H NMR, the $-CH_2$ groups on both FA and Py^+ moieties are chosen for comparison, with the area under the peak of $-CH_2$ for FA set to 2 as the standard. In ^{19}F NMR, the two $-CF_3$ groups on $TFSI^-$ are compared with that on the FA moiety with the area under the curve of the $-CF_3$ group on FA set to 3 as the standard. We also find that the two $-CF_2$ groups on the FA show

https://dx.doi.org/10.1021/jacs.0c09649
J. Am. Chem. Soc. 2020, 142, 21393−21403

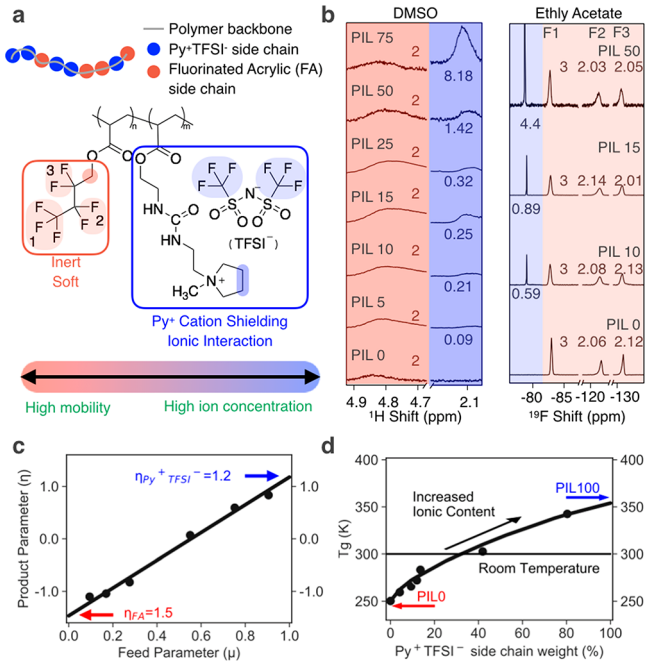

Figure 3. Chemical structure of the PIL. (a) The PIL is composed of two side chains: ionic acrylate (blue, Py^+TFSI^-) and fluorinated acrylate (red, FA). The Py^+TFSI^- side chain contains cationic "shielding" groups and increases the ionic interaction among polymer chains, while the FA is inert and improves the polymer's mobility. The shaded hydrogen groups (dark shade) and fluorine groups (light shade) are identified in the (b) NMR spectra, where the area under the identified peak was integrated to calculate the relative ratio between the two side chains. The CF_3 group in FA is marked F1, and the two other CF_2 groups are marked F2 and F3, corresponding to the numbering in part a. (c) Fitting of the feed and yield parameter FA and Py^+TFSI^- monomers using the Mayo–Lewis equation to identify their reactivity ratios (marked on the graph). (d) The glass transition temperature (Tg) of the PILs is plotted against the weight percentage of the Py^+TFSI^- side chain measured in NMR. They are fitted to the Gordon–Taylor equation, and the Tg values at 0 and 100 wt % correspond to the polymers PIL 0 (measured) and PIL 100 (calculated), respectively.

a magnitude close to 2 in the spectrum, which confirms the chemical composition of FA. In both ^1H NMR and ^{19}F NMR spectra, the PILs with higher content of Py^+TFSI^- show higher NMR peak intensity of the corresponding functionalities. Also, the calculated amount of Py^+ (^1H NMR) matches with that of $TFSI^-$ (^{19}F NMR), thus confirming the 1:1 ratio of Py^+ cation and $TFSI^-$ anion.

In addition to the chemical composition, a detailed examination of the monomer feed and polymer yield ratios of various PILs can lead to useful insights about the polymer configuration. The analysis was performed using previously reported graphical methods of fitting the feed and yield ratios using the Mayo–Lewis relationships with Fineman–Ross and Kelen–Tüdös corrections. The equations are as follows:

$$\eta = \left[r_1 + \frac{r_2}{\alpha}\right]\mu - \frac{r_2}{\alpha};\ \eta = \frac{G}{\alpha + H};\ \mu = \frac{H}{\alpha + H};\ G = \frac{f_1(2F_1 - 1)}{(1 - f_1)F_1};\ H = \frac{f_1^2(1 - F_1)}{(1 - f_1)^2 F_1};\ \alpha = \sqrt{H_{min}H_{max}}$$

Here, f_i, F_i, and r_i are the feed, yield, and reactivity percentage of the monomer; while the subscripts 1 and 2 stand for Py^+TFSI^- and FA, respectively. The details of the fitting method can be found in previous literature.[56,57] Figure 3c shows the plot of product parameter η against feed parameter μ. Combining the above-mentioned equations, we can linearly fit the product and feed parameters and find the absolute values of η at $\mu = 0$ and 1 to determine the reactivity ratios of Py^+TFSI^- and FA monomers. The identified reactivity ratios of Py^+TFSI^- and FA monomers are similar to each other and close to one, which indicates that both monomers are equally likely to react with themselves and the other monomers, and thus the configuration of the two polymer side chains is random.

To understand the morphology of the copolymer, small-angle X-ray scattering (SAXS) experiments were performed on PIL samples with various ionic contents. As shown in Supporting Information Figure 10, the scattering profiles of all these polymers have no indication of secondary structures in the polymer, revealing that the charges are uniformly distributed in the polymer.

The effect of polymer compositions on the Tg of PILs is measured with differential scanning calorimetry (DSC) and plotted against the weight percentage of the Py^+TFSI^- side chain calculated from NMR measurements (Figure 3d). As the ionic content in the polymer increases, the Tg values of the polymers rise from −15 °C to over 70 °C, which exemplifies our hypothesis that increasing ionic content leads to higher ionic interaction and polymer rigidity. The experimentally obtained Tg of the polymers is in good agreement with the Gordon–Taylor relationship[58] that predicts the Tg of random copolymers based on their weight percentage of individual side chains. The polymer Tg is related to the temperature threshold below which the segmental motion of the polymer chain is thermodynamically arrested. As an important criterion of PIL polymers at the interface is their charge-induced mobility, we determine that polymers with higher ionic content than PIL 25 will be unsuitable for room temperature battery applications as their Tg values exceed 25 °C.

Characterizations of PILs. The systematic variation of PIL copolymer composition provides an opportunity for understanding their structure–property relationships. The mechanical properties of the PILs are examined with oscillatory shear rheological measurements. Figure 4a reports the frequency-dependent storage (G') and loss (G'') modulus in the linear viscoelastic region at 25 °C that is obtained by time–temperature superposition of rheological data measured at different temperatures. We observe that, similar to the trend in the DSC measurements, increasing ionic (Py^+TFSI^-) content in the polymers leads to enhanced stiffness. The PIL 0 polymer shows the rheological response of a Newtonian liquid such that the G' and G'' decay with characteristic slopes of 1 and 2, respectively. As the ionic content increases in the PIL, the polymer modulus increases, and PIL 5, PIL 10, and PIL 15 show viscoelastic liquidlike behavior with its slope deviating from 1 and 2 at the high-frequency region. On the contrary, PIL 25 behaves like a viscoelastic solid, such that $G' > G''$ at the high-frequency range, followed by a crossover and flow behavior ($G'' > G'$) at the low-frequency range. The increased ionic content and rise in secondary ionic interaction in the polymer are attributed to the observed rise in mechanical properties in rheological measurements.

The ionic conductivity of PILs also shows significant variation as a function of the ionic content. Here, we sandwich the PILs (in the absence of additional salt and liquid) between two stainless steel electrodes and measure the bulk resistance of the

https://dx.doi.org/10.1021/jacs.0c09649
J. Am. Chem. Soc. 2020, 142, 21393−21403

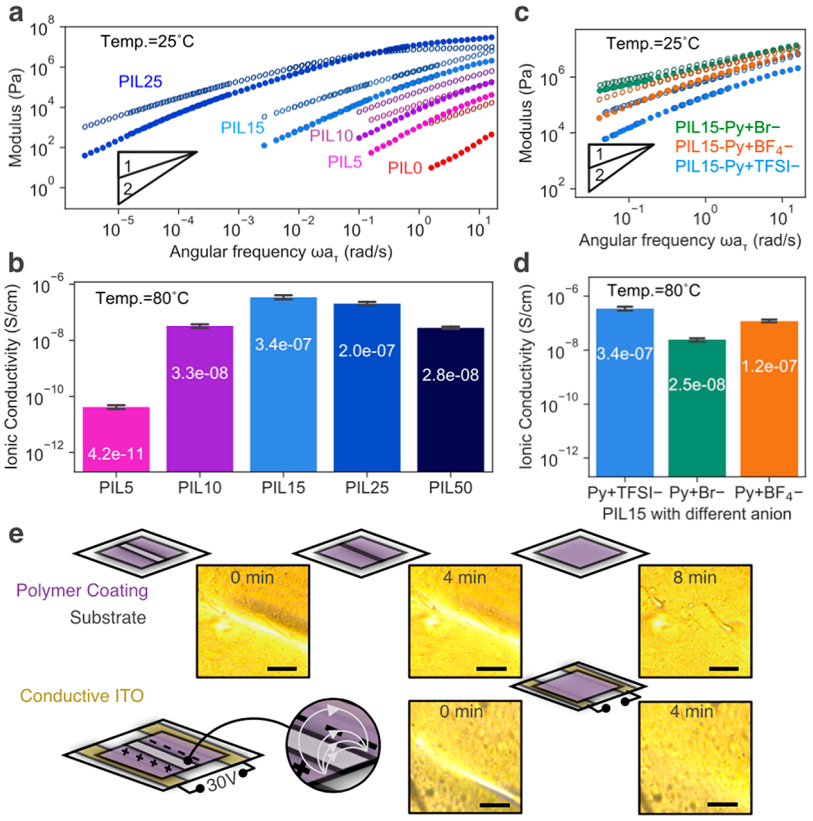

Figure 4. Physical property of the polymers: (a) rheological frequency sweep measurements of polymers with different ionic content. Storage modulus (G', filled circles) and loss modulus (G'', unfilled circles) are measured across different frequencies. The time−temperature superposition (TTS) technique was utilized to obtain a wide frequency range; they are superpositioned to the temperature of 25 °C. The characteristic slopes of 1 and 2 for G' and G'' vs frequency at the terminal relaxation region is drawn. (b) Ionic conductivities of PILs calculated based on impedance spectroscopy measurement of polymeric samples sandwiched between steel electrodes at a fixed temperature. No salt was added to the measured polymer. (c) Rheological frequency sweep measurements of PIL 15 with different anions. This measurement is conducted in accordance with the details in (a). (d) Ionic conductivities of PIL 15 with different anions (without any addition of electrolyte or salt). (e) Schematics showing the "scratch-healing behavior" of viscoelastic PIL 15 polymer and the corresponding bright-field optical microscopy image taken at different times of the healing process. The bright strip indicates the scratch with reduced thickness of the coating and increased light transmission. When the electric field is applied to the polymer through the conductive ITO substrate, the concentrated electric field at the scratch boundary accelerates the restoration process. Scale bar: 50 μm.

polymer using impedance spectroscopy at 80 °C (Supporting Information Figure 11). Unlike the polymer mechanics, the ionic conductivity does not show a monotonic relationship with the ionic content. Instead, the ionic conductivity of the PILs shows a peak in magnitude at PIL 15. It is postulated that polymers with low ionic content like PIL 5 and PIL 10 do not have sufficient amounts of dissociated mobile ions, while the polymers with higher ionic interaction like PIL 25 and PIL 50 polymers have limited segmental motion of polymer chains. The PIL 15 has the optimum ion content and sufficient polymer chain mobility, resulting in higher ionic transport.

Since the polymer coating on the lithium anode is designed to prevent side reactions between the liquid electrolyte and the electrode, its swelling behavior is of importance. The swelling test on the PIL 15 polymer showed that its weight has increased by a mere 9.1% after prolonged soaking in the electrolyte. Thus, the PIL 15 coating can essentially block the electrolyte access to lithium electrode at such a low swelling rate, as noted in an earlier study.[46] We also investigated the ionic conductivity of the PIL 15 polymer after electrolyte soaking (Supporting Information Figure 12), where we observed an increase in the ionic conductivity after the polymer is soaked in ether-based electrolytes.

The durability of the coating layer is examined by soaking a Cu foil spin coated with PIL 15 polymer in 10 mL of DOL/DME 1 M LiTFSI 1% $LiNO_3$ electrolyte for 100 h and examining the coating integrity with cross-sectional scanning electron microscopy SEM before and after. Based on Supporting Information Figure 13, the PIL 15 coating remains intact.

The mechanical property and ionic conductivity of the polymer not only depend on the ionic content but also rely on the cation−anion interactions. To examine the effect of anion chemistry on the PIL's mechanical and ionic property, we fix the ionic content to PIL 15 and the cation to Py^+ and pair it with three different anions: $TFSI^-$, BF_4^-, and Br^-. These monovalent anions have different sizes, with $TFSI^-$ being the largest and Br^- being the smallest. For the same valency, larger anions can effectively disperse the charge concentration, resulting in weak ionic interaction and lower modulus. As illustrated in Figure 4c, PIL 15 with Br^- anion (smallest in size, most concentrated ionic charge) has the highest modulus shown in the rheological measurements due to strong ionic interactions. The increased rigidity and subdued segmental motion of polymer chains also impact the ionic conductivity. As shown in Figure 4d, PIL 15 with $TFSI^-$ anion has the highest ionic conductivity, while the one with Br^- anion has the lowest conductivity. As a coating on the lithium anode surface, PIL should be optimized for

https://dx.doi.org/10.1021/jacs.0c09649
J. Am. Chem. Soc. 2020, 142, 21393−21403

maximum ionic conductivity to facilitate lithium transport and at the same time maintain high mobility for Py^+ cations for responding to any concentrated electric field on the lithium anode. Thus, we believe $TFSI^-$ anions are suitable for PIL coating that yields ideal mechanical and ionic properties.

The ionic functionalities in the PIL polymer further affect its response to an electric field such that we observed an accelerated self-healing of the PIL 15 polymer when subjected to a potential difference (Figure 4e). Due to the flowable nature of PIL 15 (Py^+TFSI^-) at room temperature, the mobility of polymer chains can "heal" a scratch on its surface in 8 min. However, this process can be expedited by two times when an electric field is applied perpendicular to the scratch on the polymer. This demonstration was done specifically on a glass substrate, where PIL 15 was coated between two parallel conductive ITO strips, and a 30 V potential was applied across the ITO electrodes, resulting in a "scratch-healing time" of 4 min, as shown in Supporting Information Video 1. As the polymer remains at room temperature, we attribute the accelerated healing of the polymer to be capacitive instead of an induction heating response of the polymer due to the electric field. We hypothesis that the ionic groups in the polymer are polarized by the imposed electric field, resulting in charge concentration across the scratch boundary. The Coulombic attraction from opposite charges facilitates the polymer chain motion causing accelerated healing of the polymer. The observed behavior showcases that the polymer chain motion can be driven and expedited by an electric potential gradient.

Electrodeposition and Battery Performance. The ability to progressively vary the mechanical and ionic properties of the PIL polymers provides an opportunity to systematically study the effects of these characteristics on lithium metal electrodeposition stability. First, we want to examine the impact of PIL coating on the Coulombic efficiency (C.E.) of lithium plating/stripping. Here, we coated Cu electrodes with different PIL polymers and characterized the C.E. in Li||Cu cell configuration with current density 0.5 mAh/cm^2 and 1 mAh/cm^2 capacity using a pre-established protocol of a modified Aurbach method.[59] The polymer-coating thickness is maintained at ~0.9 μm for different PILs (see Supporting Information Table 2). Interestingly, we found that the efficiency is the highest with the PIL 15 coating (Figure 5a), which is also the polymer with the highest ion conductivity and flowable mechanical property among other polymers in this study. In comparison, the cell with PIL 25 coating shows a lower Coulombic efficiency under the same conditions. We hypothesize that PIL 15 has a higher degree of response to morphological changes on the electrode surface, making it more effective at modulating the localized electric field by the aforementioned shielding mechanism. On the other hand, the relatively rigidity of the PIL 25 coating can limit its cationic mobility on the electrode surface. For coatings with lower ionic content (PIL 10 and PIL 0), the absence or lack of Py^+ ions in the polymers results in lower Coulombic efficiency. It is also seen that the C.E. of the PIL 0 coating is even lower than that of bare Cu electrode. This can be rationalized by the fact that PIL 0 lacks ionic conduction channels that can lead to charge buildup across the interface causing degradation of the polymer. This hypothesis is corroborated by Li||Li cell cycling data discussed later. Additionally, we also assess the C.E. when Py^+TFSI^- ionic liquid is used as a small-molecule additive in the electrolyte. The amount of Py^+TFSI^- small molecules in the electrolyte is maintained to be same as that of Py^+TFSI^- molecules in the PIL

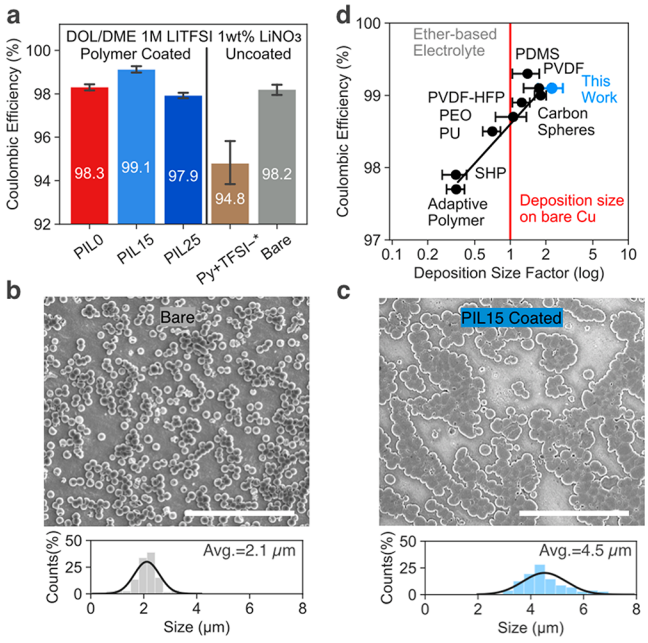

Figure 5. Coulombic efficiency and deposition morphology. (a) Coulombic efficiencies of Li||Cu cells measured at the current density 0.5 mA/cm^2 with 1 mAh/cm^2 capacity. *: 2 wt % Py^+TFSI^- ionic liquid was added to the electrolyte. SEM top-down view of deposited Li on Cu electrode at 0.1 mA/cm^2 current density for 0.1 mAh/cm^2 in DOL/DME 1 M LiTFSI 1 wt % $LiNO_3$. The Cu electrode is either (b) bare or (c) PIL 15 coated. Scale bar: 30 μm. The size distribution of lithium deposition is included and fitted to a Gaussian distribution function. The average sizes of the lithium deposition are listed. (d) The Coulombic efficiencies measured from Li||Cu cells in ether-based electrolyte from this study and previous studies[44,54,61] are plotted against the "deposition size factor" in log scale.

15 coating. Unlike being tethered to a polymer chain and physically restricted to the anode, small-molecule electrolyte additives are free to diffusion in the electrolyte. We find that the C.E. significantly dropped when small molecules of Py^+TFSI^- were introduced because of side reactions. Using impedance spectroscopy, we validated our hypothesis by showing that the small-molecule Py^+TFSI^- additive in the electrolyte increased the interface impedance in comparison to the control electrolyte (no additives), while the PIL 15 coating maintained similar interfacial impedance compared to the control (Supporting Information Figure 14). The interfacial impedance of the Li||Li symmetric cell with PIL 15 coating stabilized around 300 ohms after 100 h, as revealed by electrochemical impedance spectra (EIS) in Supporting Information Figure 15. The Coulombic efficiency of Li||Cu cells with and without PIL 15 coating is also characterized in 1 M LiPF6 EC/DEC electrolyte, where the addition of the PIL 15 coating layer improved the measured C.E. (Supporting Information Figure 16).

We further analyzed the electrodeposition morphology using scanning electron microscopy (SEM) after plating 0.1 mAh/cm^2 lithium metal on copper electrode with and without the PIL 15 coating in a Li||Cu cell. Lithium nuclei deposited on bare Cu substrates have an average diameter of 2.1 μm, as shown in Figure 5b. In comparison, deposition on PIL 15 coated Cu electrode shows larger lithium nuclei, with an average diameter of 4.5 μm (Figure. 5c). For each sample, the size average and distribution of the lithium nuclei are extracted from over 100 nuclei and multiple measurements. The detailed measurement

https://dx.doi.org/10.1021/jacs.0c09649
J. Am. Chem. Soc. 2020, 142, 21393−21403

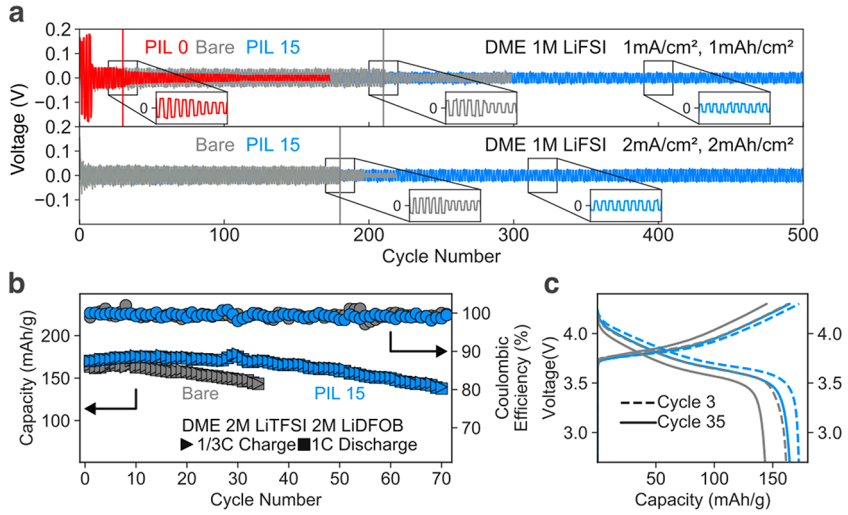

Figure 6. Long-term electrochemical characterization. (a) Strip and plate of Li||Li cells over cycles with coated/uncoated Li electrodes (red, PIL0 coated; blue, PIL15 coated; gray, bare Li). (b) Li||NMC 532 cell cycling with either PIL 15 coated (blue) or bare (gray) 25 μm Li foil and (c) the charge and discharge voltage plotted against capacity for Li||NMC cells at cycle 3 and 35.

method on nuclei size extraction can be found in Supporting Information Figure 17. Lithium deposition morphology is also investigated in the same electrolyte (DOL/DME 1 M LiTFSI 1 wt % $LiNO_3$, Supporting Information Figure 18) with higher deposition capacity (1 mAh) and in another ether-based electrolyte (DME 1 M LiFSI, Supporting Information Figure 19). For both cases, SEM images show that the deposited lithium under the PIL 15 coating has regular granule, in contrast to the fibrous structure of lithium deposited on bare Cu electrode.

To understand the lithium deposition morphology when the pressure is not exerted to the deposited lithium, a Li||Cu cell with PTFE ring spacer is assembled to avoid the pressure from the separator. As shown in Supporting Information Figure 20, with the presence of the PIL 15 polymeric coating, deposited lithium exhibits granular regular morphology, and the lack of PIL 15 polymer coating showcases dendritic lithium deposition structures.

The improved morphology is derived from the cationic shielding effect of PIL polymer coating blanketing the lithium deposition underneath (Supporting Information Figure 21). To validate this hypothesis, the lithium depositions on PIL 15 coated and Li-deposited Cu electrodes were analyzed using X-ray photoelectron spectroscopy (XPS) along with Ar ion sputtering. Careful analysis of the XPS depth profiling result shows that the top layer of the electrode is dominated by carbon−fluorine bonds (−CF_2/−CF_3, ~688 eV, F 1s, ~299 eV, C 1s), carbon−oxygen bonds (−C−O/−C═O, ~287 eV, C 1s, ~532 eV, O 1s), and carbon−carbon bonds (−C−C, ~285 eV, C 1s), confirming the presence of the polymer layer on top of the lithium deposition. Argon sputtering of the sample indicated a SEI layer underneath the polymer, as revealed by the detection of lithium−fluorine bonds (−LiF, ~685 eV, F 1s, 55.5 eV, Li 1s) and lithium−oxygen bonds (−Li−O, 529 eV, O 1s, ~54 eV, Li 1s). Further sputtering showed signals of lithium metal bond (−Li, ~53 eV, Li 1s), supporting the hypothesis that lithium deposition occurs beneath the polymer-coating layer. We also validate this hypothesis using cross-sectional SEM images showing the layer of PIL 15 coating on top of deposited lithium (Supporting Information Figure 22).

To understand the role of PIL coating on the lithium deposition, we measured the exchange current density of lithium deposition with and without the presence of PIL 15 coating using a microelectrodes setup. The exchange current density describes the rate of electron transfer at zero overpotential. By performing at a high-rate cyclic voltammetry scan on the microelectrode, the mass-transfer-related limit is lifted, enabling us to observe the reaction kinetics of the system. Without the presence of a polymeric coating, the exchange current density is measured at 33.9 mA/cm^2, similar to past values reported in a similar setup and electrolyte (Supporting Information Figure 23).[54,60] With a layer of dip-coated PIL 15 coating on the electrode, the exchange current is dropped by threefold, indicating that the reaction rate on the electrode surface has been reduced. With a layer of nonionic coating (PIL 0) on the surface, the lithium ion has a limited pathway to conduct through the coating, and the mass transfer limit of the surface has been reached. The microelectrode exchange current density measurement has showcased that ionic units in the polymer (PIL 15) are the main channel for lithium conduction through the coating. When lithium is effectively transported through the coating, the presence of ionic shielding units like Py^+ lowers the reaction kinetics of lithium deposition and thus lowers the exchange current density.

To quantify the effect of PIL 15 coating on lithium morphology, we utilize a nondimensional number of "deposition size factor", which is defined as the ratio between the deposition size in the presence of a coating and that of a bare Cu electrode. We find that the PIL coating results in a deposition size factor of 2.14 (4.5 μm/2.1 μm), corresponding to an increment in deposition size by over two times. We extend this size change analysis to previous studies of polymeric[54,61] and micro-structure[44] interfaces on lithium metal anode in ether-based electrolytes and correlate the deposition size factor to the measured C.E. Figure 5d shows that the increase in Coulombic efficiency is directly related to the lithium deposition size. The deposition size factor is plotted in a logarithmic scale to accommodate a wide range of the values, and the deposition size when no coating is applied is marked by the line when the size factor is one. Details of the deposition and C.E. measurements for all the previous studies displayed are listed in Supporting

https://dx.doi.org/10.1021/jacs.0c09649
J. Am. Chem. Soc. 2020, 142, 21393−21403

Information Table 3. For samples with the size factor larger than one (increase in lithium deposition size), the C.E. approaches or surpasses 99%, with the PIL 15 coating having one of the highest size factors and C.E. This indicates that the incorporation of Py^+ cation in the polymer is an effective interfacial strategy toward large lithium deposition structure and improved Coulombic efficiency.

To evaluate the long-term cycle stability of the PIL 15 coating on lithium surfaces, we performed galvanostatic charge and discharge tests in symmetric lithium cells. We found that the PIL 15 were capable of maintaining stable cycling of the batteries for over 500 cycles both at 1 and 2 mA/cm^2 current densities, while cells with bare lithium failed in 200 cycles. As shown in Figure 6a, the zoomed-in window of the voltage profile around the cycles of cell failure exhibit a decrease in operation voltage, indicative of cell failure by a short-circuit event. We also analyzed the battery performance using the PIL 0 coating and observed that the symmetric cells experience close to 0.2 V overpotentials in the initial stages of cycling, followed by an abrupt drop in the voltage profile associated with short-circuiting or interfacial breakdown at 20 cycles. Due to the absence of any ionic groups in the PIL 0, the lithium transport across the interface is impeded, resulting in the observed high overpotentials in the initial cycles and eventual failure.

The PIL 15 coating is examined in the Li||NMC full cells, where the polymer is applied to a 25 μm (5 mAh/cm^2) thin lithium anode foil and paired against a NMC532 anode with 2.7 mAh/cm^2 capacity. The battery is cycled in the voltage range of 2.7 and 4.3 V. In comparison to cells with bare lithium anodes, the battery with PIL 15 coated anode shows higher retention of battery capacity (Figure 6b). The lifetime of the battery can be determined by the number of cycles taken for the cell to reach 80% of its original capacity. The cell with PIL 15 coated anode has a lifetime close to 70 cycles, whereas the uncoated anode's lifetime is registered to be about 35 cycles. The voltage profiles of the coated and uncoated Li||NMC cell at cycle 3 and 35 are displayed in Figure 6c, showcasing that the cell with PIL 15 polymer coated Li anode has lower overpotential than without. Similar observation of improved cycle life with coating was found in three replicated pairs of coated/uncoated Li||NMC cells (Supporting Information Figure 24).

CONCLUSION

In conclusion, we have shown that organic salts based on pyrrolidinium cations (Py^+TFSI^-) have reduction potentials (−3.17 V vs SHE) lower than that of Li/Li$^+$. This provides a design strategy for a polymer interface that incorporates such organic salts to resist electrochemical breakdown, while promoting lithium ion transport and modulating the charge transfer process at the electrode surface. We simultaneously incorporate low Tg fluorinated alkyl side chains in the polymer architecture to provide flowability on the electrode surface and at the same time to prevent interfacial side reactions with the bulk electrolyte. The polymer dynamics and the ion transport in these polymeric materials are shown to be dependent on the supramolecular ionic interactions that can be tuned by the tethered ion content or anion chemistry. We further show that the cationic polymer responds to any external electric field stimulus that enables a unique "shielding mechanism" of suppressing morphological instabilities during Li deposition, resulting in enhanced battery lifetime and Coulombic efficiency. This mechanism differs from previously reported polymer interfaces, which were based on strategies like formation of stable SEI by Li−polymer reaction,[47,62] high Li$^+$ transference number interface,[46,48] or controlled release of SEI forming salt additives.[31,53] We believe that the polymer design concept reported in this work can be synergistically combined with previous strategies to develop highly stable electrode−electrolyte interfaces to further boost the performance of lithium metal batteries.

EXPERIMENTAL SECTION

Materials Synthesis and Characterizations. Most chemicals used for synthesizing ionic liquids and polymers, as well as all salts and electrolytes used for battery cycling, were acquired from Sigma-Aldrich except for 1*H*,1*H*-heptafluorobutyl acrylate (CAS: 424-64-60) which was purchased from Oakwood Chemical and 2-isocyanatoethyl acrylate (CAS: 13641-96-8) which was obtained from TCI. NMC532 electrodes were provided by the CAMP facility at Argonne National Laboratories.

Ionic liquids were synthesized by reacting uncharged molecules with propyl iodide, and detailed synthesis procedures can be found in the Supporting Information (Supporting Information Figures 1−2). The random copolymers were synthesized by radical polymerization of both ionic and fluorinated monomers in dimethylformamide (DMF). Comprehensive synthesis procedures of monomers and polymers are shown in the Supporting Information (Supporting Information Figures 3−5, Table 1).

The chemical structures of the polymers were characterized with proton nuclear magnetic resonance spectroscopy (500 MHz, D-DMSO), fluorine nuclear magnetic resonance spectroscopy (400 MHz, ethyl acetate), and Fourier-transform infrared spectroscopy (Thermo Nicolet iS500). Glass transition temperatures (Tgs) of the polymers were measured with differential scanning calorimetry (TA Q2000) using heat−cool−heat profile between −50 and 200 °C (10 °C/min heating, 5 °C/min cooling). Frequency sweeps (0.1−100 Hz) were performed on each polymer sample at different temperatures (25−95°C) with a TA ARES G2 rheometer to obtain frequency-dependent storage and loss moduli and time−temperature superposition.

To characterize polymers' electrochemical properties, we coated the polymers on both Cu and Li surfaces. On Cu foils (1 cm diameter), a polymer solution (0.1 g/mL ethyl acetate) was spin-coated at 2000 rad/min speed and dried in a 70 °C vacuum oven for 3 h. Li metal chips or 20 μm Li foils (1 cm^2) were dip-coated in an Ar-filled glovebox with 330 mg/mL ethyl acetate polymer solutions before being dried on a hot plate at 70 °C for 3 h.

The ionic conductivity of the polymer was measured with biologic VMP3 system by impedance spectroscopy measurements over a frequency range from 100 mHz to 7 MHz. The polymers measured were sandwiched by two steel electrodes. The geometry of the polymeric samples was controlled as a cylinder with 1 cm^2 cross-sectional area and 0.36 mm thickness.

The swelling of the polymer was examined by soaking the polymer in 3-dioxolane (DOL) 1,2- dimethoxyethane (DME) (volume ratio 1:1) electrolyte for 2 h. After 2 h of soaking, the polymer was extracted from the electrolyte and dried for 10 s. The weight difference before and after the soaking was recorded, and the swelling rate of the polymer is calculated as the weight increase after soaking divided by the weight of the polymer before soaking.

Seal-healing measurement of the polymer was conducted on a 1 mm thick polymer layer formed by solution cast between two parallel lithium titanate (LTO) electrodes lying on the substrate with a gap of 1 cm. A voltage of 30 V was applied across the electrodes. The cut was made with a standard scalpel. Pictures/videos of the polymer self-healing process were taken under a microscope at 2.5× magnification.

The XPS and SEM measurements were performed on the deposited lithium at the Cu foil electrode. The deposition profile is revealed in the electrochemical characterization section. After the Li was deposited on the Cu electrode, the Cu electrode was extracted from the Li||Cu cell in an Ar-filled glovebox. The foil was then rinsed in DME electrolyte for 10 min to remove excess salts and then dried for 2 min. The XPS profile was collected with PHI VersaProbe 3 XPS probe with an Al K-alpha

https://dx.doi.org/10.1021/jacs.0c09649
J. Am. Chem. Soc. 2020, 142, 21393−21403

source. The air-sensitive lithium sample was transferred from the Ar glovebox to the XPS measurement station in an airtight vessel to prevent any air exposure at all times. The depth profile of the XPS was conducted in combination with Ar ion sputtering at 2 kV 1uA on a 0.2 mm × 0.2 mm surface. The SEM sample was transferred from the glovebox to the FEI Magellan 400 XHR SEM through an airtight vessel. The lithium sample experienced a short period of air exposure when transferring from the airtight vessel to the SEM chamber before the chamber was pumped to 10^{-6} bar vacuum. The size of deposited lithium nuclei was measured with ImageJ software from more than 100 nuclei.

Electrochemical Characterization and Testing Profiles. The reduction potentials of different organic ionic liquids were performed in a three-electrode beaker cell (cathode, anode, Ag reference electrode), with voltage sweeping from 0 to −6 V at a rate of 100 mV/s. We made three different types of cells (Li||Cu, Li||Li, and Li||NMC) for this study. All coin cells used a 1 cm diameter single-layer Celgard 2325 separator. The Coulombic efficiency of Li||Cu cells was tested using a modified Aurbach method.[59] The cell was first cycled between 0 and 1 V at 20 μA cm^{-2} for 10 cycles to clear out any impurity on the surface. Then 5 mAh cm^{-2} of Li was plated, followed by 10 cycles of plate and stripping at 0.5 mA for 1 mAh before finally being stripped to 1 V. Eighty microliters of 1 M lithium bis(trifluoromethanesulphonyl) imide (LiTFSI) 1,3-dioxolane (DOL) 1,2- dimethoxyethane (DME) (volume ratio 1:1) and 1 wt % lithium nitrate ($LiNO_3^-$) electrolyte was used for Coulombic efficiency measurements. The same electrolyte is also used in the Li||Cu cell for XPS and SEM characterizations of deposited lithium on Cu foil. For the XPS and SEM measurements, the cell was first cycled between 0 and 1 V at 20 μA cm^{-2} for 10 cycles, and then the voltage was lowered to 0 V at 0.1 mA cm^{-2} to eliminate the capacitive effect near the Cu substrate. Then 0.1 mAh cm^{-2} lithium metal was coated on the substrate at the current density of 0.1 mA cm^{-2}. All Li||Cu cells were rested 8 h before testing. Strip and plate testing of Li||Li cells was conducted at both 1 and 2 $mAhcm^{-2}$ current density, plating and stripping for 1 h each cycle. Impedance spectroscopy was measured on Li||Li cells with a frequency sweep from 0.07 Hz to 7 MHz. The electrolyte for the Li||Li cell is 80 μL of DME 1 M LiFSI, and the cells were rested for 1 h before testing. The Li||NMC full cells were composed of 1 cm^2 coated 20 μL thin Li foils and 1 cm^2 2.0 mAh/cm^2 lithium nickel cobalt manganese oxide NMC 532 cathode with 2 M LiTFSI and 2 M lithium difluoro(oxalato)borate (LiDFOB) in DME. All LI||NMC cells were rested 8 h before cycling. They were tested between 2.7 and 4.3 V by first precycling at C/10 for 2 cycles and then cycling at 1/3 C charging and 1 C discharge.

■ ASSOCIATED CONTENT

Supporting Information

The Supporting Information is available free of charge at https://pubs.acs.org/doi/10.1021/jacs.0c09649.

Materials synthesis and NMR spectra of poly(ionic liquid) PIL, SEM images, XPS spectra, EIS spectra, in situ optical observation of the deposited lithium film and PIL 15 coated electrodes, and full cell cycling data (PDF)

Video of PIL 15 coated between two parallel conductive ITO strips with a 30 V potential applied across the ITO electrodes (MOV)

■ AUTHOR INFORMATION

Corresponding Authors

Snehashis Choudhury − *Department of Chemical Engineering, Stanford University, Stanford, California 94305, United States*; Email: sc2563@stanford.edu

Yi Cui − *Department of Materials Science and Engineering, Stanford University, Stanford, California 94305, United States; Stanford Institute for Materials and Energy Sciences, SLAC National Accelerator Laboratory, Menlo Park, California 94025, United States*; orcid.org/0000-0002-6103-6352; Email: yicui@stanford.edu

Zhenan Bao − *Department of Chemical Engineering, Stanford University, Stanford, California 94305, United States*; orcid.org/0000-0002-0972-1715; Email: zbao@stanford.edu

Authors

Zhuojun Huang − *Department of Materials Science and Engineering, Stanford University, Stanford, California 94305, United States*; orcid.org/0000-0001-6236-8693

Huaxin Gong − *Department of Chemical Engineering, Stanford University, Stanford, California 94305, United States*; orcid.org/0000-0002-2493-0793

Complete contact information is available at: https://pubs.acs.org/10.1021/jacs.0c09649

Author Contributions

⊥These authors contributed equally to this work

Notes

The authors declare no competing financial interest.

■ ACKNOWLEDGMENTS

Z.H. acknowledges support by the American Association of University Women international fellowship. S.C. acknowledges support by the Battery 500 Consortium Program Young Investigator Award. The work was supported by the Assistant Secretary for Energy Efficiency and Renewable Energy, Office of Vehicle Technologies of the U.S. Department of Energy under the Battery 500 Consortium program. Part of this work was performed at the Stanford Nano Shared Facilities (SNSF), supported by the National Science Foundation under award ECCS-1542152. Z.H. thanks H.-C. Wu for helpful discussion and experimental assistance regarding the SAXS measurement.

■ REFERENCES

(1) Whittingham, M. S. History, Evolution, and Future Status of Energy Storage. *Proc. IEEE* **2012**, *100* (SpecialCentennial Issue), 1518−1534.

(2) Nishi, Y. Performance of the First Lithium Ion Battery and Its Process Technology. *Lithium Ion Batteries* **1998**, 181−198.

(3) Dunn, B.; Kamath, H.; Tarascon, J.-M. Electrical Energy Storage for the Grid: A Battery of Choices. *Science* **2011**, *334* (6058), 928−935.

(4) Cano, Z. P.; Banham, D.; Ye, S.; Hintennach, A.; Lu, J.; Fowler, M.; Chen, Z. Batteries and Fuel Cells for Emerging Electric Vehicle Markets. *Nat. Energy* **2018**, *3* (4), 279−289.

(5) Schmuch, R.; Wagner, R.; Hörpel, G.; Placke, T.; Winter, M. Performance and Cost of Materials for Lithium-Based Rechargeable Automotive Batteries. *Nat. Energy* **2018**, *3* (4), 267−278.

(6) Goodenough, J. B.; Park, K.-S. The Li-Ion Rechargeable Battery: A Perspective. *J. Am. Chem. Soc.* **2013**, *135* (4), 1167−1176.

(7) Whittingham, M. S. Lithium Batteries and Cathode Materials. *Chem. Rev.* **2004**, *104* (10), 4271−4302.

(8) Lin, D.; Liu, Y.; Cui, Y. Reviving the Lithium Metal Anode for High-Energy Batteries. *Nat. Nanotechnol.* **2017**, *12* (3), 194−206.

(9) Tikekar, M. D.; Choudhury, S.; Tu, Z.; Archer, L. A. Design Principles for Electrolytes and Interfaces for Stable Lithium-Metal Batteries. *Nat. Energy* **2016**, *1* (9), 16114.

(10) Cheng, X.-B.; Zhang, R.; Zhao, C.-Z.; Zhang, Q. Toward Safe Lithium Metal Anode in Rechargeable Batteries: A Review. *Chem. Rev.* **2017**, *117* (15), 10403−10473.

(11) Kim, H.; Jeong, G.; Kim, Y.-U.; Kim, J.-H.; Park, C.-M.; Sohn, H.-J. Metallic Anodes for next Generation Secondary Batteries. *Chem. Soc. Rev.* **2013**, *42*, 9011−9034.

(12) Aurbach, D.; McCloskey, B. D.; Nazar, L. F.; Bruce, P. G. Advances in Understanding Mechanisms Underpinning Lithium−air Batteries. *Nat. Energy* **2016**, *1* (9), 16128.
(13) Bruce, P. G.; Freunberger, S. a; Hardwick, L. J.; Tarascon, J.-M. Li-O2 and Li-S Batteries with High Energy Storage. *Nat. Mater.* **2012**, *11* (1), 19−29.
(14) Zheng, J.; Kim, M. S.; Tu, Z.; Choudhury, S.; Tang, T.; Archer, L. A. Regulating Electrodeposition Morphology of Lithium: Towards Commercially Relevant Secondary Li Metal Batteries. *Chem. Soc. Rev.* **2020**, *49* (9), 2701−2750.
(15) Cheng, X.; Zhang, R.; Zhao, C.; Wei, F.; Zhang, J.; Zhang, Q. Solid Electrolyte Interphases: A Review of Solid Electrolyte Interphases on Lithium Metal Anode. *Adv. Sci.* **2016**, *3* (3), 1−20.
(16) Xu, K. Electrolytes and Interphases in Li-Ion Batteries and Beyond. *Chem. Rev.* **2014**, *114* (23), 11503−11618.
(17) Tarascon, J. M.; Armand, M. Issues and Challenges Facing Rechargeable Lithium Batteries. *Nature* **2001**, *414* (6861), 359−367.
(18) Niu, C.; Pan, H.; Xu, W.; Xiao, J.; Zhang, J.-G.; Luo, L.; Wang, C.; Mei, D.; Meng, J.; Wang, X.; Liu, Z.; Mai, L.; Liu, J. Self-Smoothing Anode for Achieving High-Energy Lithium Metal Batteries under Realistic Conditions. *Nat. Nanotechnol.* **2019**, *14* (6), 594−601.
(19) Yang, C.-P.; Yin, Y.-X.; Zhang, S.-F.; Li, N.-W.; Guo, Y.-G. Accommodating Lithium into 3D Current Collectors with a Submicron Skeleton towards Long-Life Lithium Metal Anodes. *Nat. Commun.* **2015**, *6* (1), 8058.
(20) Zhang, H.; Liao, X.; Guan, Y.; Xiang, Y.; Li, M.; Zhang, W.; Zhu, X.; Ming, H.; Lu, L.; Qiu, J.; Huang, Y.; Cao, G.; Yang, Y.; Mai, L.; Zhao, Y.; Zhang, H. Lithiophilic-Lithiophobic Gradient Interfacial Layer for a Highly Stable Lithium Metal Anode. *Nat. Commun.* **2018**, *9* (1), 3729.
(21) Zhang, Y.; Luo, W.; Wang, C.; Li, Y.; Chen, C.; Song, J.; Dai, J.; Hitz, E. M.; Xu, S.; Yang, C.; Wang, Y.; Hu, L. High-Capacity, Low-Tortuosity, and Channel-Guided Lithium Metal Anode. *Proc. Natl. Acad. Sci. U. S. A.* **2017**, *114* (14), 3584−3589.
(22) Ye, H.; Xin, S.; Yin, Y.-X.; Guo, Y.-G. Advanced Porous Carbon Materials for High-Efficient Lithium Metal Anodes. *Adv. Energy Mater.* **2017**, *7* (23), 1700530.
(23) Zhang, R.; Chen, X.; Shen, X.; Zhang, X.-Q.; Chen, X.-R.; Cheng, X.-B.; Yan, C.; Zhao, C.-Z.; Zhang, Q. Coralloid Carbon Fiber-Based Composite Lithium Anode for Robust Lithium Metal Batteries. *Joule* **2018**, *2* (4), 764−777.
(24) Liu, Y.; Lin, D.; Jin, Y.; Liu, K.; Tao, X.; Zhang, Q.; Zhang, X.; Cui, Y. Transforming from Planar to Three-Dimensional Lithium with Flowable Interphase for Solid Lithium Metal Batteries. *Sci. Adv.* **2017**, *3* (10), eaao0713.
(25) Yan, K.; Sun, B.; Munroe, P.; Wang, G. Three-Dimensional Pie-like Current Collectors for Dendrite-Free Lithium Metal Anodes. *Energy Storage Mater.* **2018**, *11*, 127−133.
(26) Ren, X.; Chen, S.; Lee, H.; Mei, D.; Engelhard, M. H.; Burton, S. D.; Zhao, W.; Zheng, J.; Li, Q.; Ding, M. S.; Schroeder, M.; Alvarado, J.; Xu, K.; Meng, Y. S.; Liu, J.; Zhang, J. G.; Xu, W. Localized High-Concentration Sulfone Electrolytes for High-Efficiency Lithium-Metal Batteries. *Chem.* **2018**, *4* (8), 1877−1892.
(27) Qian, J.; Henderson, W. a; Xu, W.; Bhattacharya, P.; Engelhard, M.; Borodin, O.; Zhang, J.-G. High Rate and Stable Cycling of Lithium Metal Anode. *Nat. Commun.* **2015**, *6*, 6362.
(28) Chen, S.; Zheng, J.; Mei, D.; Han, K. S.; Engelhard, M. H.; Zhao, W.; Xu, W.; Liu, J.; Zhang, J.-G. High-Voltage Lithium-Metal Batteries Enabled by Localized High-Concentration Electrolytes. *Adv. Mater.* **2018**, *30* (21), 1706102.
(29) Cao, X.; Ren, X.; Zou, L.; Engelhard, M. H.; Huang, W.; Wang, H.; Matthews, B. E.; Lee, H.; Niu, C.; Arey, B. W.; Cui, Y.; Wang, C.; Xiao, J.; Liu, J.; Xu, W.; Zhang, J.-G. Monolithic Solid−electrolyte Interphases Formed in Fluorinated Orthoformate-Based Electrolytes Minimize Li Depletion and Pulverization. *Nat. Energy* **2019**, *4* (9), 796−805.
(30) Choudhury, S.; Archer, L. A. Lithium Fluoride Additives for Stable Cycling of Lithium Batteries at High Current Densities. *Adv. Electron. Mater.* **2016**, *2*, 1500246.
(31) Liu, Y.; Lin, D.; Li, Y.; Chen, G.; Pei, A.; Nix, O.; Li, Y.; Cui, Y. Solubility-Mediated Sustained Release Enabling Nitrate Additive in Carbonate Electrolytes for Stable Lithium Metal Anode. *Nat. Commun.* **2018**, *9* (1), 3656.
(32) Li, W.; Yao, H.; Yan, K.; Zheng, G.; Liang, Z.; Chiang, Y.-M.; Cui, Y. The Synergetic Effect of Lithium Polysulfide and Lithium Nitrate to Prevent Lithium Dendrite Growth. *Nat. Commun.* **2015**, *6* (May), 7436.
(33) Zhang, X.-Q.; Cheng, X.-B.; Chen, X.; Yan, C.; Zhang, Q. Fluoroethylene Carbonate Additives to Render Uniform Li Deposits in Lithium Metal Batteries. *Adv. Funct. Mater.* **2017**, *27* (10), 1605989.
(34) Choudhury, S.; Tu, Z.; Stalin, S.; Vu, D.; Fawole, K.; Gunceler, D.; Sundararaman, R.; Archer, L. A. Electroless Formation of Hybrid Lithium Anodes for Fast Interfacial Ion Transport. *Angew. Chem., Int. Ed.* **2017**, *56* (42), 13070−13077.
(35) Zhang, S. S. A Review on Electrolyte Additives for Lithium-Ion Batteries. *J. Power Sources* **2006**, *162* (July), 1379−1394.
(36) Zheng, J.; Engelhard, M. H.; Mei, D.; Jiao, S.; Polzin, B. J.; Zhang, J.-G.; Xu, W. Electrolyte Additive Enabled Fast Charging and Stable Cycling Lithium Metal Batteries. *Nat. Energy* **2017**, *2*, 17012.
(37) Choudhury, S.; Wan, C. T.; Al Sadat, W. I.; Tu, Z.; Lau, S.; Zachman, M. J.; Kourkoutis, L. F.; Archer, L. A. Designer Interphases for the Lithium-Oxygen Electrochemical Cell. *Sci. Adv.* **2017**, *3* (4), e1602809.
(38) Zhang, J.; Sun, B.; Zhao, Y.; Tkacheva, A.; Liu, Z.; Yan, K.; Guo, X.; McDonagh, A. M.; Shanmukaraj, D.; Wang, C.; Rojo, T.; Armand, M.; Peng, Z.; Wang, G. A Versatile Functionalized Ionic Liquid to Boost the Solution-Mediated Performances of Lithium-Oxygen Batteries. *Nat. Commun.* **2019**, *10* (1), 602.
(39) Amanchukwu, C. V.; Kong, X.; Qin, J.; Cui, Y.; Bao, Z. Nonpolar Alkanes Modify Lithium-Ion Solvation for Improved Lithium Deposition and Stripping. *Adv. Energy Mater.* **2019**, *9* (41), 1902116.
(40) Yu, Z.; Wang, H.; Kong, X.; Huang, W.; Tsao, Y.; Mackanic, D. G.; Wang, K.; Wang, X.; Huang, W.; Choudhury, S.; Zheng, Y.; Amanchukwu, C. V.; Hung, S. T.; Ma, Y.; Lomeli, E. G.; Qin, J.; Cui, Y.; Bao, Z. Molecular Design for Electrolyte Solvents Enabling Energy-Dense and Long-Cycling Lithium Metal Batteries. *Nat. Energy* **2020**, *5*, 526−533.
(41) Kozen, A. C.; Lin, C.; Pearse, A. J.; Schroeder, M. a; Han, X.; Hu, L.; Lee, S.; Rubloff, G. W.; Noked, M. Next-Generation Lithium Metal Anode Engineering via Atomic Layer Deposition. *ACS Nano* **2015**, *9* (6), 5884−5892.
(42) Li, N.-W.; Yin, Y.-X.; Yang, C.-P.; Guo, Y.-G. An Artificial Solid Electrolyte Interphase Layer for Stable Lithium Metal Anodes. *Adv. Mater.* **2016**, *28* (9), 1853−1858.
(43) Tu, Z.; Choudhury, S.; Zachman, M. J.; Wei, S.; Zhang, K.; Kourkoutis, L. F.; Archer, L. A. Fast Ion Transport at Solid−solid Interfaces in Hybrid Battery Anodes. *Nat. Energy* **2018**, *3*, 310−316.
(44) Zheng, G.; Lee, S. W.; Liang, Z.; Lee, H.-W.; Yan, K.; Yao, H.; Wang, H.; Li, W.; Chu, S.; Cui, Y. Interconnected Hollow Carbon Nanospheres for Stable Lithium Metal Anodes. *Nat. Nanotechnol.* **2014**, *9* (8), 618−623.
(45) Lin, D.; Liu, Y.; Chen, W.; Zhou, G.; Liu, K.; Dunn, B.; Cui, Y. Conformal Lithium Fluoride Protection Layer on Three-Dimensional Lithium by Nonhazardous Gaseous Reagent Freon. *Nano Lett.* **2017**, *17* (6), 3731−3737.
(46) Yu, Z.; Mackanic, D. G.; Michaels, W.; Lee, M.; Pei, A.; Feng, D.; Zhang, Q.; Tsao, Y.; Amanchukwu, C. V.; Yan, X.; Wang, H.; Chen, S.; Liu, K.; Kang, J.; Qin, J.; Cui, Y.; Bao, Z. A Dynamic, Electrolyte-Blocking, and Single-Ion-Conductive Network for Stable Lithium-Metal Anodes. *Joule* **2019**, *3* (11), 2761−2776.
(47) Gao, Y.; Yan, Z.; Gray, J. L.; He, X.; Wang, D.; Chen, T.; Huang, Q.; Li, Y. C.; Wang, H.; Kim, S. H.; Mallouk, T. E.; Wang, D. Polymer−inorganic Solid−electrolyte Interphase for Stable Lithium Metal Batteries under Lean Electrolyte Conditions. *Nat. Mater.* **2019**, *18* (4), 384−389.
(48) Tu, Z.; Choudhury, S.; Zachman, M. J.; Wei, S.; Zhang, K.; Kourkoutis, L. F.; Archer, L. A. Designing Artificial Solid-Electrolyte

https://dx.doi.org/10.1021/jacs.0c09649
J. Am. Chem. Soc. 2020, 142, 21393−21403

Interphases for Single-Ion and High-Efficiency Transport in Batteries. *Joule* **2017**, *1* (2), 394−406.
(49) Choudhury, S.; Stalin, S.; Vu, D.; Warren, A.; Deng, Y.; Biswal, P.; Archer, L. A. Solid-State Polymer Electrolytes for High-Performance Lithium Metal Batteries. *Nat. Commun.* **2019**, *10* (1), 1−8.
(50) Zheng, G.; Wang, C.; Pei, A.; Lopez, J.; Shi, F.; Chen, Z.; Sendek, A. D.; Lee, H.-W.; Lu, Z.; Schneider, H.; Safont-Sempere, M. M.; Chu, S.; Bao, Z.; Cui, Y. High-Performance Lithium Metal Negative Electrode with a Soft and Flowable Polymer Coating. *ACS Energy Lett.* **2016**, *1* (6), 1247−1255.
(51) Stalin, S.; Tikekar, M.; Biswal, P.; Li, G.; Johnson, H. E. N.; Deng, Y.; Zhao, Q.; Vu, D.; Coates, G. W.; Archer, L. A. Designing Polymeric Interphases for Stable Lithium Metal Deposition. *Nano Lett.* **2020**, *20* (8), 5749−5758.
(52) Ding, F.; Xu, W.; Graff, G. L.; Zhang, J.; Sushko, M. L.; Chen, X.; Shao, Y.; Engelhard, M. H.; Nie, Z.; Xiao, J.; Liu, X.; Sushko, P. V.; Liu, J.; Zhang, J.-G. Dendrite-Free Lithium Deposition via Self-Healing Electrostatic Shield Mechanism. *J. Am. Chem. Soc.* **2013**, *135* (11), 4450−4456.
(53) Choudhury, S.; Stalin, S.; Vu, D.; Warren, A.; Deng, Y.; Biswal, P.; Archer, L. A. Solid-State Polymer Electrolytes for High-Performance Lithium Metal Batteries. *Nat. Commun.* **2019**, *10* (1), 4398.
(54) Lopez, J.; Pei, A.; Oh, J. Y.; Wang, G.-J. N.; Cui, Y.; Bao, Z. Effects of Polymer Coatings on Electrodeposited Lithium Metal. *J. Am. Chem. Soc.* **2018**, *140* (37), 11735−11744.
(55) Kwon, T.-w.; Choi, J. W.; Coskun, A. Prospect for Supramolecular Chemistry in High-Energy-Density Rechargeable Batteries. *Joule* **2019**, *3* (3), 662−682.
(56) Mayo, F. R.; Lewis, F. M. Copolymerization. I. A Basis for Comparing the Behavior of Monomers in Copolymerization; The Copolymerization of Styrene and Methyl Methacrylate. *J. Am. Chem. Soc.* **1944**, *66* (9), 1594−1601.
(57) Kelen, T.; Tüdös, F.; Turcsányi, B. Confidence Intervals for Copolymerization Reactivity Ratios Determined by the Kelen-Tüdös Method. *Polym. Bull.* **1980**, *2* (1), 71−76.
(58) Gordon, M.; Taylor, J. S. Ideal Copolymers and the Second-Order Transitions of Synthetic Rubbers. I. Non-Crystalline Copolymers. *J. Appl. Chem.* **1952**, *2* (9), 493−500.
(59) Adams, B. D.; Zheng, J.; Ren, X.; Xu, W.; Zhang, J.-G. Accurate Determination of Coulombic Efficiency for Lithium Metal Anodes and Lithium Metal Batteries. *Adv. Energy Mater.* **2018**, *8* (7), 1702097.
(60) Shi, F.; Pei, A.; Vailionis, A.; Xie, J.; Liu, B.; Zhao, J.; Gong, Y.; Cui, Y. Strong Texturing of Lithium Metal in Batteries. *Proc. Natl. Acad. Sci. U. S. A.* **2017**, *114* (46), 12138−12143.
(61) Liu, K.; Pei, A.; Lee, H. R.; Kong, B.; Liu, N.; Lin, D.; Liu, Y.; Liu, C.; Hsu, P.; Bao, Z.; Cui, Y. Lithium Metal Anodes with an Adaptive "Solid-Liquid" Interfacial Protective Layer. *J. Am. Chem. Soc.* **2017**, *139* (13), 4815−4820.
(62) Gao, Y.; Rojas, T.; Wang, K.; Liu, S.; Wang, D.; Chen, T.; Wang, H.; Ngo, A. T.; Wang, D. Low-Temperature and High-Rate-Charging Lithium Metal Batteries Enabled by an Electrochemically Active Monolayer-Regulated Interface. *Nat. Energy* **2020**, *5*, 534−542.

https://dx.doi.org/10.1021/jacs.0c09649
J. Am. Chem. Soc. 2020, 142, 21393−21403